Research Article | Vol. 13, No. 7 / 1 Jul 2022 / Biomedical Optics Express 4007
Biomedical Optics EXPRESS

Line-scanning SD-OCT for *in-vivo*, non-contact, volumetric, cellular resolution imaging of the human cornea and limbus

LE HAN,[1,7] BINGYAO TAN,[1,2,3,4,7] ZOHREH HOSSEINAEE,[1,5] LIN KUN CHEN,[1] DENISE HILEETO,[6] AND KOSTADINKA BIZHEVA[1,5,6,*]

[1]*Department of Physics and Astronomy, University of Waterloo, Waterloo, Ontario N2L 3G1, Canada*
[2]*School of Chemical and Biomedical Engineering, Nanyang Technological University, 637460, Singapore*
[3]*SERI-NTU Advanced Ocular Engineering (STANCE), 639798, Singapore*
[4]*Singapore Eye Research Institute, Singapore National Eye Center, 169856, Singapore*
[5]*Department of Systems Design Engineering, University of Waterloo, Waterloo, Ontario N2L 3G1, Canada*
[6]*School of Optometry and Vision Science, University of Waterloo, Waterloo, Ontario N2L 3G1, Canada*
[7]*Contributed equally*
[*]*kbizheva@uwaterloo.ca*

Abstract: *In-vivo*, non-contact, volumetric imaging of the cellular and sub-cellular structure of the human cornea and limbus with optical coherence tomography (OCT) is challenging due to involuntary eye motion that introduces both motion artifacts and blur in the OCT images. Here we present the design of a line-scanning (LS) spectral-domain (SD) optical coherence tomography system that combines $2 \times 3 \times 1.7$ µm (x, y, z) resolution in biological tissue with an image acquisition rate of ~2,500 fps, and demonstrate its ability to image *in-vivo* and without contact with the tissue surface, the cellular structure of the human anterior segment tissues. Volumetric LS-SD-OCT images acquired over a field-of-view (FOV) of 0.7 mm × 1.4 mm reveal fine morphological details in the healthy human cornea, such as epithelial and endothelial cells, sub-basal nerves, as well as the cellular structure of the limbal crypts, the palisades of Vogt (POVs) and the blood microvasculature of the human limbus. LS-SD-OCT is a promising technology that can assist ophthalmologists with the early diagnostics and optimal treatment planning of ocular diseases affecting the human anterior eye.

1. Introduction

Corneal and limbal inherited, degenerative, and infectious pathologies constitute the 4th leading cause of blindness worldwide after cataract, glaucoma, and age-related macular degeneration [1]. The accurate and early diagnostics of corneal and limbal pathologies and the effective planning of therapies are strongly dependent on the ability of imaging technologies to visualize, identify, and characterize the tissue cellular structure *in-vivo.* Currently, the only clinical imaging method that can image corneal and limbal cells *in-vivo* is In-vivo Confocal Microscopy (IVCM) [2]. However, IVCM has a number of limitations: a) in order to generate high resolution enface images, IVCM requires physical contact with the corneal epithelium that necessitates corneal anesthesia, and significantly increases the risk of corneal infections and abrasions; b) limited field of view (FOV ~400 µm × 400 µm); and c) difficulty generating high resolution volumetric images due to depth location ambiguity associated with poor axial resolution, as well as slow scanning in the axial direction compared to fast axial eye motion.

Compared to IVCM, optical coherence tomography (OCT) offers the advantages of *in-vivo,* non-contact, high-resolution, high-speed, volumetric imaging of the cornea [3,4]. OCT technology with different optical designs has been used to image *in-vivo* the cellular structure of the human and animal cornea. Point-scanning spectral-domain (SD) OCT can achieve axial resolution in the order of 1 µm in corneal tissue by using broadband lasers [5–10]. Although *in-vivo* volumetric

#465916 https://doi.org/10.1364/BOE.465916
Journal © 2022 Received 7 Jun 2022; accepted 8 Jun 2022; published 17 Jun 2022

Biomedical Optics EXPRESS

SD-OCT images of the corneal cellular structure have been reported in the past from anesthetized animals [10,11], where anesthesia was used to reduce image artifacts induced by involuntary eye motion, *in-vivo* imaging of the human cornea remained problematic due to the limited acquisition speed of the linear array camera. Recently, *in-vivo* volumetric SD-OCT images of the human cornea acquired with a 250 kHz linear array camera showing the cellular structure of all corneal layers were reported [12], however, motion artifacts were still noticeable in the 3D images.

Full-field (FF) time-domain (TD) OCT utilizes a different scanning approach where enface images are acquired rapidly while the imaged object is scanned slowly in the axial direction [13–15]. The relative insensitivity of the images to optical aberrations, combined with a transverse resolution of ~1 µm, allows FF-TD-OCT to image the cells in the human corneal stroma and endothelium both *ex-vivo* [16–18] and *in-vivo* [19,20]. While FF-TD-OCT was able to resolve the superficial cells in the corneal epithelium, and image the Palliades of Vogt (POV) and the blood vasculature in the limbus, the technology was not able to resolve the basal and wing cells in the corneal epithelium and the cellular structure of the limbal crypts, most likely due to the limited dynamic range of the area camera used, resulting in limited SNR [20].

FF swept-source (SS) OCT technology was introduced recently for *in-vivo* human corneal imaging [21]. FF-SS-OCT uses a rapidly tunable light source and offers better sensitivity and a significantly faster volumetric acquisition rate. Although the concept of FF-SS-OCT was published a while ago [22], it took many years of development of fast area cameras before FF-SS-OCT could be developed for *in-vivo* imaging of the human eye [21,23–27]. One major advantage of FF-SS-OCT is the high phase stability in the enface images, which allows for wavefront aberration correction with digital adaptive optics (DAO) [28–32]. However, the fairly narrow spectral range of the tunable lasers currently limits the FF-SS-OCT axial resolution in corneal tissue to ~5 µm, which is insufficient for visualization of cellular details in the axial direction.

Line-scanning (LS) SD-OCT offers an alternative design to point-scanning SD-OCT, that utilizes line instead of point illumination optical beam projected onto the imaged object, an area camera instead of a linear array camera, and 1D scanning instead of 2D scanning to achieve image acquisition rates higher than 2,000 fps. LS-SD-OCT generates B-scan images of the imaged object by sampling the lateral structure of the object in one direction of the 2D camera while encoding the axial structure of the object by projecting spectral information in the orthogonal direction of the camera, followed by Fourier transformation of the spectral data into the spatial domain. Therefore, the B-scan rate of LS-SD-OCT is determined by the frame rate of the 2D camera, while the spatial resolution of LS-SD-OCT is determined by the spectrum of the light source (axial direction) and the imaging optics (lateral direction). Because LS-SD-OCT utilizes a spatially extended light source, the optical power of the imaging beam can be increased safely by ~4× compared to the optical imaging power used in point-scanning SD-OCT for *in-vivo* human cornea imaging. This safe increase of the optical power compensates partly for the loss of sensitivity in LS-SD-OCT resulting from the faster image acquisition rates. Although the concept of LS-SD-OCT was published nearly 2 decades ago [33], the use of this technology for *in-vivo* imaging of the human retinal structure and blood flow [34] and the retinal response to visual stimulation [35] was only reported recently. However, the LS-SD-OCT technology used in those studies offered limited axial OCT resolution of ~ 6.2 µm in air, which is insufficient to visualize cells and sub-cellular structures in the axial direction.

Here we present a novel design of an LS-SD-OCT system that combines a $2 \times 3 \times 1.7$ µm ($x \times y \times z$) resolution in biological tissue with an acquisition rate of ~2,500 fps and a depth scanning range of ~1.3 mm. We also demonstrate the ability of the system to image *in-vivo*, volumetrically, and without contact with the tissue surface, the cellular structure of the human cornea and limbus.

Biomedical Optics EXPRESS

2. Methods

2.1. Design of the LS-SD-OCT system

The schematic of the LS-SD-OCT is shown in Fig. 1. A cartesian coordinate (*x,y,z*) system is used to describe the imaging system; x-direction refers to the beam scanning direction, y-direction is along the line illumination direction, and z-direction denotes the beam propagating direction. The system is powered by a femtosecond laser (Integral, Femtolasers GmbH) with a 785 nm center wavelength and 129 nm spectral bandwidth measured at 3 dB height. A spool of 100-meter long fiber is used to stretch the femtosecond pulses and simulate CW emission. The light is first collimated by an achromatic doublet lens L1 (AC127-019-B, Thorlabs), and the $1/e^2$ beam diameter of the output beam is 3.21 mm. A telecentric pair of lenses L2 (AC254-060-B, Thorlabs) and L3 (AC254-100-B, Thorlabs) form a beam expander with magnification factor of 1.67. The beam's circular symmetry breaks after passing through an achromatic cylindrical lens CL1 (ACY254-100-B, Thorlabs). A 50:50 non-polarizing beamsplitter (BS014, Thorlabs) serves as the core of the OCT interferometer and separates the incident beam into the sample and reference arms of the interferometer.

In the sample arm, the beam is focused in in the yz-plane at the center of a 1-D galvanometer scanner (GVS011, Thorlabs). A telecentric pair of achromat doublets, L4 and L5 (AC254-075-B, Thorlabs) placed after the scanner is used to relay the beam to the entrance of a microscope objective (M Plan Apo NIR 10×/0.26, Mitutoyo). The incident power on the sample surface is 2.6 mW, which is below the maximum permissible exposure for both human cornea and retina according to the ANSI standard [35]. In the reference arm, the optical beam is reshaped to a circular collimated beam by a second cylindrical lens CL2 (ACY254-100-B, Thorlabs) and then focused onto a mirror with lens L6 (AC254-060-B, Thorlabs). A neutral density filter (NDF) is used to control the optical power, while a pair of BK7 prisms is used for hardware dispersion compensation (DC).

Light scattered from the sample and reflected from the reference mirror interfere at the beamsplitter and is projected onto a custom spectrometer through a telecentric pair of lenses L7 (AC254-150-B, Thorlabs) and L8 (AC254-100-B, Thorlabs). An adjustable slit (VA100C, Thorlabs) is placed in between L7 and L8 to block stray light. The spectrometer is comprised of a volume phase holographic grating (960 lp/mm @ 840nm, Wasatch Photonics), a camera lens (Planar T* 1.4/85, Zeiss), and a 2D complementary metal-oxide semiconductor (CMOS) camera (Dimax S4, PCO). The spectrum is dispersed in the spectral (horizontal) direction of the camera, and the spatial information of the sample along the y-direction is projected in the spatial (vertical) direction of the camera. While the full size of the CMOS sensor is 2016×2016 pixels with a pixel size of 11×11 μm^2, with the current optical design of the LS-SD-OCT system, only an area of 1920×800 (spectral × spatial) is illuminated. This area corresponds to a maximum camera read-out rate of 2.5 kHz. The data acquisition trigger and scanner waveform are generated and synchronized through a data acquisition (DAQ) card (PCIe-6321, NI). A custom Labview program is used to control the B-scan live display, the 3D image acquisition, and data saving.

2.2. Imaging procedure

Images of the human central cornea and corneoscleral limbus were acquired *in-vivo* with the LS-SD-OCT system from healthy subjects. The imaging sessions were approved by the University of Waterloo Office of Research Ethics and informed consent was obtained from the subjects. A custom head support frame, mounted on XYZ translation stages, was used to stabilize the subject's head during the imaging procedure and align ocular locations of interest with respect to the OCT imaging probe. A fixation target was used for additional eye alignment with respect to the imaging beam and for reducing involuntary eye motion. Volumetric (800 A-scans × 600 B-scans × 1920 pixels) images were acquired. The system's design and scanning protocol allowed

Biomedical Optics EXPRESS

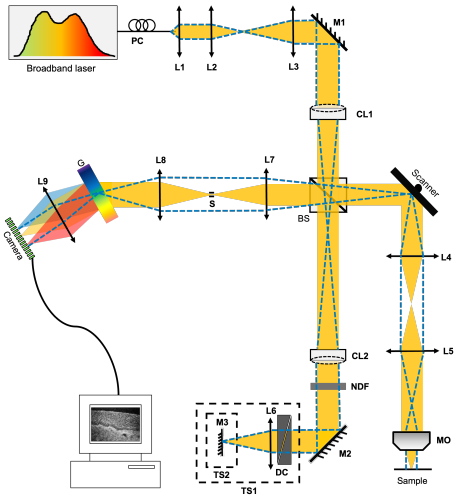

Fig. 1. Schematic of the LF-SD-OCT system. Horizontal and vertical orientations of the optical beam are represented by the solid yellow and the blue dashed lines respectively. BS, non-polarizing beam splitter; CL, cylindrical lens; G, transmission grating; DC, dispersion compensator; L, lens; M, mirror; MO, microscope objective; NDF, neutral density filter; PC, polarization controller; S, slit; TS, translational stage.

for the acquisition of a single 3D tomogram with a field of view (FOV) of 0.7 mm × 1.4 mm (x × y) and 1.3 mm depth scanning range in free space. The maximum camera frame rate for this setting was 2461 fps, resulting in an equivalent B-scan rate of ~2.5 kHz and volumetric data acquisition time of 0.24 s. Because of the microscope objective's limited depth-of-focus, the anterior and posterior cornea were imaged separately, and the reference optical path length was adjusted accordingly.

2.3. Image processing

Images were generated from the raw OCT data and numerically dispersion compensated up to the 4th order with a custom MATLAB algorithm. The B-scan and enface images shown were averaged over 3 adjacent images and convoluted with a Gaussian filter if necessary for better visualization. The volumetric images were generated with Amira (Thermo Fisher Scientific). Note that as the intensity of the optical beam along the line (y-direction) has Gaussian distribution and the cornea is not flat, the edges of the enface LS-SD-OCT images generated from the 3D stacks were of significantly lower SNR compared to the central region. For this reason, the LS-SD-CT enface images were trimmed from 700 µm × 1400 µm to 700 µm × 700 µm.

2.4. Maximum permissible exposure for in-vivo anterior segment ocular imaging with the LS-SD-OCT

During the *in-vivo* image acquisition, the imaging beam forms a line shape along the y-direction on the cornea or limbus, and the line is scanned in the x-direction. The line-shaped optical beam projected onto the cornea will generate an elliptical power distribution at the retina, whose minor axis in the y-direction is much shorter than its major axis in the x-direction. The ellipse's shift in x-direction during scanning is negligible compared to the length of its major axis, and the exposure should be considered static at the retinal surface. Therefore, we limit the exposure time to no longer than 10 seconds, which is the typical time period between successive blinks for normal blinking rate in the healthy eye.

Biomedical Optics EXPRESS

The $1/e^2$ beam diameter of the light intensity distribution at the objective's focal plane is 3.8 μm in the x-direction and 1.00 mm in the y-direction. According to the American National Standards Institute (ANSI) guidelines, ANSI Z80.36-2016 [36], the Group 1 unweighted anterior segment visible and infrared radiation irradiance limit value (E^{MPE}_{VIR-AS}) for a continuous wave is:

$$E^{MPE}_{VIR-AS} = \sum_{380}^{1200} = E_\lambda \times \Delta\lambda = 4\text{W/cm}^2. \tag{1}$$

The average irradiance of the system at the anterior segments is:

$$E_{VIR-AS} = \frac{P}{A} = \frac{2.6\text{mW}}{\frac{\pi}{4}1\text{mm}^2} = 0.33\text{W/cm}^2 \tag{2}$$

where A is the area of a circle with diameter of 1.0 mm. Thus, the unweighted anterior segment irradiance is only 1/12 of the group 1 maximum permission exposure (MPE) at the worst scenario of continuous illumination.

Assumming that the human eye's focal length in healthy normal adults is ~17 mm and there are no optical aberrations, the $1/e^2$ diameter of the light intensity distribution on the retina is about 19.9 µm in the y-direction. As it is smaller than 0.03 mm, we use 0.03 mm as the minor axis length. We estimate the length of the major axis at the retinal surface is ~5.1 mm based on a Zemax simulation of the LS-SD-OCT system and an eye model provided by Zemax [37]. The limit of weighted retinal visible and infrared radiation irradiance (E^{MPE}_{VIR-R}) for time-limited instruments in the time range (0.25 s, 200 s) is:

$$E^{MPE}_{VIR-R} = \sum_{380}^{1400} E_\lambda \times R(\lambda) \times \Delta\lambda = 6t^{-1/4}\text{W/cm}^2. \tag{3}$$

The weighted maximum permissible exposure for duration of 10 seconds is:

$$P^{MPE}_{VIR-R}|_{t=10\text{ s}} = E^{MPE}_{VIR-R}|_{t=10\text{ s}} \times A = 4.0\text{ mW} \tag{4}$$

where A is the area of an ellipse with a minor and major length of 0.03 mm and 5.1 mm. In addition, most energy of light source used in the LS-SD-OCT system is confined in the spectral range of (700 nm, 900 nm), in which the thermal hazard weighting function $R(\lambda)$ is less than one, so the power limit should be higher than 4.0 mW.

With a stricter standard [38], for a non-circular exposed retinal field, the maximum permissible radiant power (in Watts) is calculated as:

$$MP\Phi = 6.93 \times 10^{-4} C_T(\lambda) C'_E P^{-1}(\lambda) t^{-1/4}. \tag{5}$$

Here, $C_T(\lambda) = 10^{0.002(\lambda-700)}$ and $P(\lambda) = 1$ in the wavelength range (700 nm,1050 nm), and $C_T(\lambda) = 1$ and $P(\lambda) = 10^{-0.0074(\lambda-700)}$ in the range (600 nm, 700 nm). $C_E{}' = 8\alpha_L/\pi(\alpha_{min} + \alpha_{max})$ is a parameter for a slit field, where α_{min}=1.5 mrad, α_{max}=100 mrad, and α_L=300 mrad. Since both $C_T(\lambda)$ and $P^{-1}(\lambda)$ is not less than 1 in most regions of the spectrum, maximum permissible radiant power for duration of 10 seconds is:

$$MP\Phi > 6.93 \times 10^{-4} C'_E 10^{-1/4} = 2.9 \times 10^{-3}\text{ W} = 2.9\text{ mW}. \tag{6}$$

For the *in-vivo* human imaing studies described here, the imaging power of the LS-SD-OCT system was set to 2.6 mW, which is below the limits calculated above.

Biomedical Optics EXPRESS

3. Results

3.1. System's resolution and sensitivity

Performance test results of the LS-SD-OCT system are summarized in Fig. 2. Figure 2 (A) shows the normalized sample and reference spectra measured at the detection end of the LS-SD-OCT system by using a silver-protected mirror as the test sample. The spectra were averaged over 50 consecutive frame recordings to reduce temporal fluctuations. Since the cylindrical lens (CL1) generates a line with Gaussian power distributions along the line, for consistency, the system's axial point spread function (PSF) and signal to noise ratio (SNR) were evaluated at the central position of the line. Figure 2(B) shows the theoretical axial PSF (red line) and the axial PSF with hardware dispersion compensation only (blue line) and after additional software dispersion compensation (black line) up to the 4th order. The measured axial resolution is 2.4 μm in air, which corresponds to 1.7 μm in biological tissue, assuming an average refractive index of 1.38. Figure 2(C) shows the depth-dependent SNR measurement results. For 2.6 mW power incident on the imaged sample, the system provides an SNR of ~92 dB at an imaging depth of 100 μm away from the zero-delay and a 6 dB SNR rolloff over a range of ~0.78 mm. The system's lateral resolution was evaluated by imaging a standard United States Air Force (USAF) resolution target (Fig. 2(D)), and the measured LS-SD-OCT resolution was ~2 μm in the x-direction and ~3 μm in the y-direction.

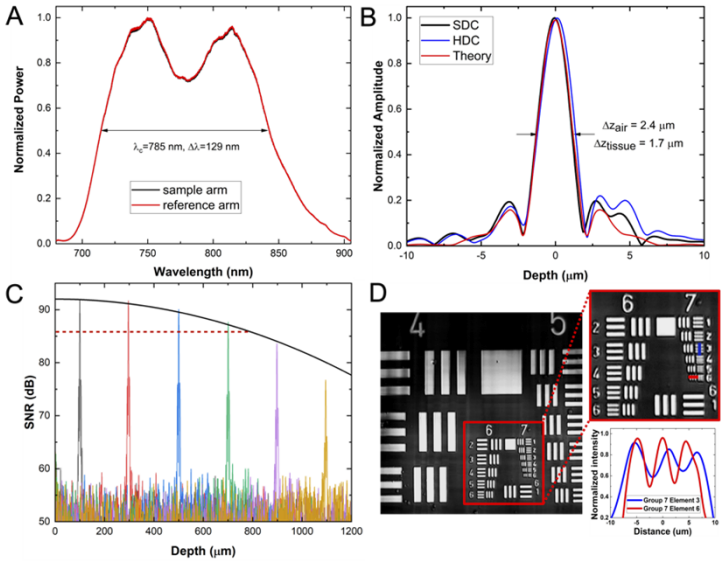

Fig. 2. System characterization results for the LS-SD-OCT system. (A) Reference (red) and sample (black) arm spectra measured at the detection end of the system. (B) Theoretical axial PSF and the axial PSF measured at a depth of 100 μm in free space with hardware (HDC) and software dispersion compensation (SDC). (C) Depth-dependent SNR and the fitted SNR rolloff. (D) Image of a USAF resolution target with intensity analysis (insert).

3.2. Cornea images

Anterior cornea images were acquired from a location slightly inferior relative to the corneal apex to avoid the strong back-reflections in the OCT images from the corneal surface. Posterior cornea images were acquired near the corneal apex. Representative images from the anterior and posterior cornea are shown in Fig. 3. A custom algorithm was used to flatten the images to correct the curvature of the anterior cornea. A volumetric image of the anterior human cornea (Fig. 3(A))

Biomedical Optics EXPRESS

shows the cellular structure of the corneal epithelium and stroma and the reflective structures in the tear film (orange arrows) that could be cellular debris, mucin clusters, or dust particles. A representative B-scan from the 3D image stack is shown in Fig. 3(B), where the cellular structure of the epithelium is visible. This B-scan image and following enface images were generated by averaging 3 adjacent images for better visualization. A cross-section of a sub-basal nerve (red arrow) located at the interface of the basal cell layer of the corneal epithelium and the Bowman's membrane, as well as reflections from keratocytes (blue arrows) in the anterior stroma are also visible. A representative Haemotoxylin and Eosin histological image of the human cornea that was acquired from a healthy normal donor human cornea postmortem (Fig. 3(C)) shows similar features. An enface image of the corneal epithelium (Fig. 3(D)) shows the cellular structure of that layer over a FOV of 700 µm × 700 µm. Figure 3(E) and Fig. 3(F) show zoomed views of the regions of interest (ROIs) in the corneal epithelial layer marked with blue and red dashed lines.

Figure 3(G) shows an enface image of the sub-basal corneal nerves located between the epithelial basal cell layer and the Bowman's membrane. Figure 3(H) and Fig. 3(I) show a large FOV and the magnified ROI of the anterior stroma, respectively. The hyper-reflective structures observed in the images correspond to keratocyte nuclei that are located in between the collagen lamellae of the corneal stroma.

Figure 3(J) shows a large FOV (700 µm × 700 µm) enface image of the corneal endothelium generated by using maximum intensity projection. The cellular mosaic of the endothelial layer is clearly visible. Figures 3(K) and 3(L) show magnified views of the ROIs in the corneal endothelium images marked with the blue and red dashed squares. The hexagonal shape of the endothelial cells is clearly visible in Fig. 3(K) and Fig. 3(L). The dark spots observed inside the endothelial cells in Fig. 3(L) (yellow arrows) most likely correspond to reflections from the cellular nuclei.

3.3. Limbus images

Volumetric images of the healthy human limbus were also acquired with the LS-SD-OCT system from the inferior limbus. The corneoscleral limbus is about a 1-2 mm wide ring-shape region of tissue that separates anatomically the peripheral cornea from the conjunctiva and sclera. The limbus has a rich and complex morphology [39–41] with dense innervation [42] and vascularization [43,44], that provides a unique environment for housing the limbal stem cells (LSCs), which are responsible for the regeneration of the corneal epithelium [44–46]. The limbus contains radially oriented fibro-vascular ridges, known as the palisades of Vogt (POVs) that are interspaced by the limbal crypts (LC).

Figure 4(A) shows the location of the inferior limbus from which LS-SD-OCT images were acquired. Figure 4(B) shows a representative B-scan from the volumetric stack. The image shows clearly the folds of the POV, as well as the cellular structure of the limbal crypts located between neighboring POVs. The image also shows the microvasculature of collagen-based tissue below the POVs and the limbal crypts. Figure 4(C) shows a magnified view of the ROI marked with yellow line in Fig. 4(B). The magnified view shows that there are highper-reflective morphological features located directly under the folds of each POV. The LS-SD-OCT image in Fig. 4(C) shows excellent correlation with a typical H&E histological cross-sectional image of the healthy limbus that was acquired from a post-mortem tissue sample.

A volumetric image of the inferior limbus (Fig. 5(A)) shows the finger-like POVs (orange arrows) and the cellular structure of the limbal crypts. The vascular network in the underlying sclera is also visible. A representative B-scan from the volumetric stack (Fig. 3(B)) shows cross-sections of the POVs and the LC. A magnified view of the ROI marked with the red dashed line in Fig. 5(B) is shown in Fig. 5(C). The cellular structure of the limbal crypt is visible. Hyper-reflective structures (yellow arrow) are visible along parts of the inner surface of the limbal crypts, which most likely correspond to clusters of melanocytes located along the

Biomedical Optics EXPRESS

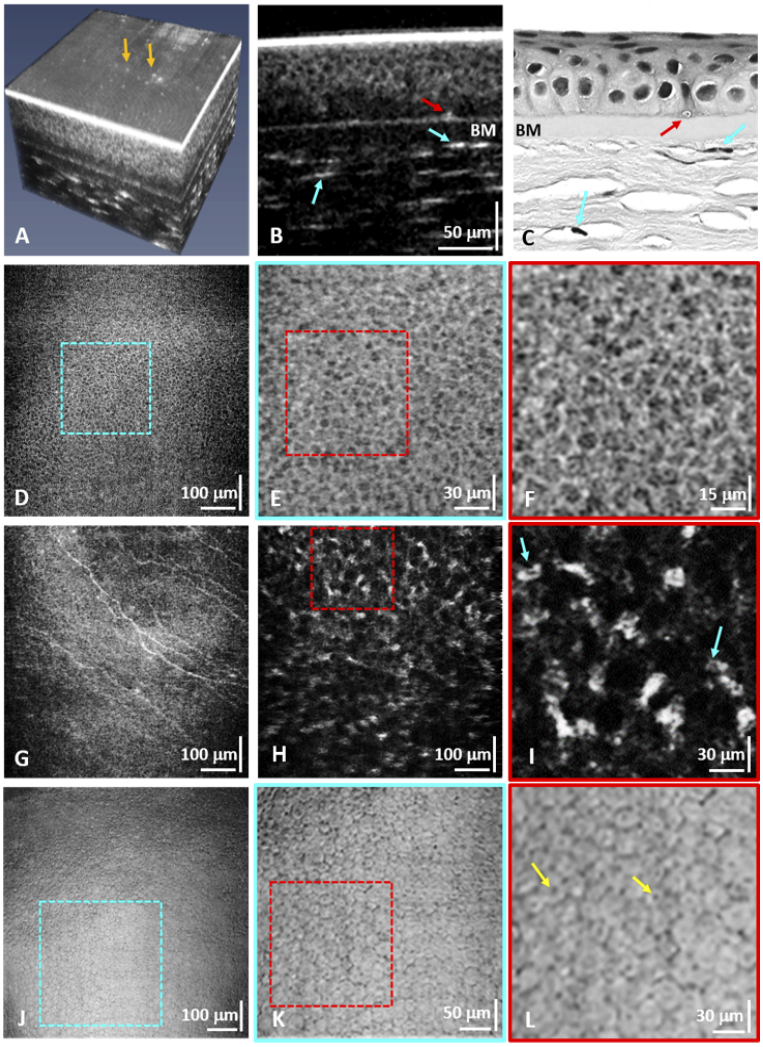

Fig. 3. (A) Flattened 3D LS-SD-OCT image of the anterior cornea from a healthy volunteer. (B) Cross-sectional image of the anterior cornea showing the cellular structure of the epithelium, the Bowman's membrane, cross-sections of sub-basal corneal nerves (red arrow), and keratocyte nuclei in the anterior stroma (blue arrows). The same morphological features are resolved in the cross-sectional H&E corneal histology *ex-vivo* (C). (D) Enface image of the corneal epithelium with magnified views (E, F) of the regions of interest (ROIs) marked with the blue and red dashed lines that show individual epithelial cells. (G) Enface images of sub-basal corneal nerves. (H, I) Enface images of the anterior stroma showing keratocyte nuclei. (J) Enface maximum intensity projection image of the corneal endothelium. (K, L) Zoomed ROIs showing individual endothelial cells.

Biomedical Optics EXPRESS

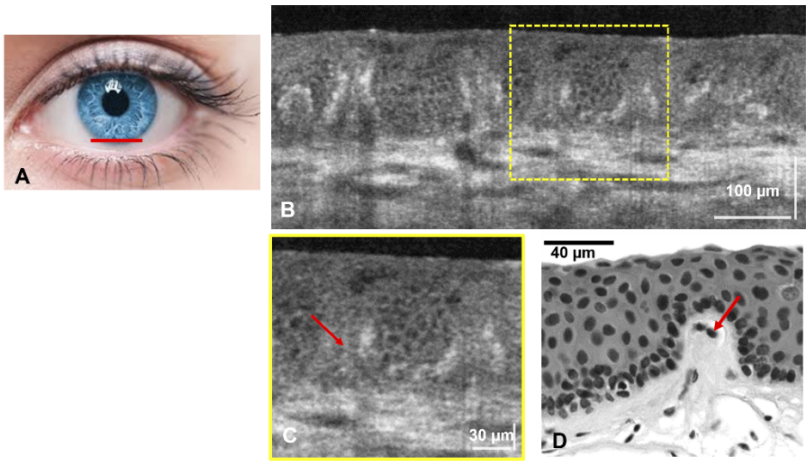

Fig. 4. (A) Human healthy inferior limbus (imaged location marked with red line). (B) Cross-sectional LS-SD-OCT image that shows the POVs and the cellular structure of the limbal crypts located in between the POVs. (C) Magnified view of the ROI marked with yellow line in (B). (D) H&E histological image of the a single palisade and the surrounding limbal crypts.

interface between the POVs and the LC. Another type of hyper-reflective structure is visible in cross-sections of the POVs, marked with red arrows in Fig. 5(B) and Fig. 5(C). These structures appear as thin, reflective lines located under the folds of the POVs and oriented vertically along the length of the POVs. Based on anatomical data, we speculate that these maybe reflections from capillaries that loop in vertical direction under the folds of the POVs, or peripheral corneal nerves that also run under the folds of the POVs.

A magnified view of the ROI marked with the yellow dashed line in Fig. 5(B) is shown in Fig. 5(D). Cells of smaller size (blue arrow) are observed close to the walls of the limbal crypts compared to cells populating the central part of the crypts. Enface images of the limbus at different depths from the same volumetric stack are shown in Fig. 5(E)–5(H). A magnified view of the ROI marked with the red dashed line in Fig. 5(E) is shown in Fig. 5(F). The cellular structure of the limbal crypt is clearly visible. Hyper-reflective linear morphological features located under the folds of the POVs and extending radially along the POVs are observed in Fig. 5(E)–5(G) (red arrows). According to anatomy data these reflective structures may correspond to blood vessels or peripheral corneal nerves. Focal stromal projections (vertical type of POVs) are observed at the interface between the limbus and the peripheral cornea (Fig. 5(G), green arrow). The image in Fig. 5(H) corresponds to a depth location at the base of the POVs and the interface of the underlying scleral tissue. It shows similar hyper-reflective liner structures along the POVs as observed in Fig. 5(E)–5(G)(red arrows).

Biomedical Optics EXPRESS

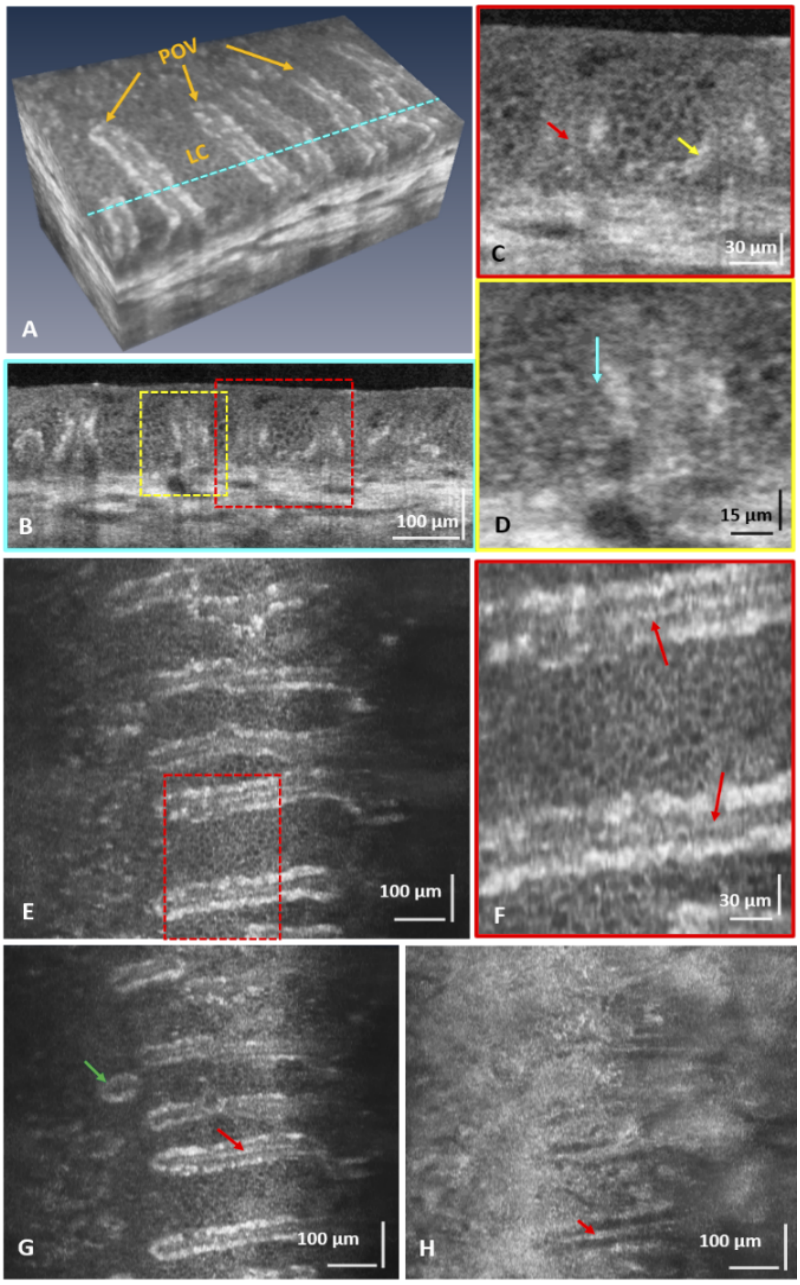

Fig. 5. (A) Flattened volumetric image of the healthy inferior human limbus showing the palisades of Vogt (POVs) and the cellular structure of the limbal crypts (LC). (B) Cross-sectional image of the POVs and the LC corresponding to the location in (A) marked with the blue dashed line. (C, D) Zoomed images of the ROIs marked in (B) that show pigmented cells along the inner borders of the limbal crypts (yellow arrow), hyper-reflective structure under the POVs (red arrow), and small sized cells, probably limbal stem cells or transient amplifying cells, located along the crypt walls (blue arrow). (E, G, and H) Enface images of the POVs and LC acquired at different depth locations. (F) Zoomed view of the ROI marked in (E). These images show a focal stromal projection (green arrow) and hyper-reflective line structures, possibly blood vessels or nerves, located under the POVs (red arrows).

Biomedical Optics EXPRESS

4. Discussion

Different OCT modalities have been used to image the corneal cells of human or animals. For example, the point-scanning micro-OCT showed excellent *ex-vivo* images of the corneal epithelial cells, keratocytes, and endothelial cells of animals [47], and the image quality is close to that achieved with IVCM. The major limitation of point-scanning SD-OCT for *in-vivo* imaging of the human corneal and limbal cells stems from the fact that the slow image acquisition rate cannot suppress image artefacts arising from involuntary eye motion (e.g., saccades), even using the fastest commercially available or research-grade linear array cameras [12,48,49]. Therefore, it can only be used to image small FOV otherwise the cellular structure in the OCT images shows blur due to eye motion. FF-TD-OCT has been used to image *in-vivo* the sub-basal nerves, keratocytes, and endothelial cells of the human cornea [19,20], and its variant, termed curved-field OCT, extended the lateral FOV to 1.13×1.13 mm in imaging the endothelium layer [50]. However, low axial resolution (~7 μm) and enface image acquisition rate (275 frames/second) limit its application for *in-vivo* 3D imaging, and the low SNR (74 dB after image averaging) prevented visualization of the corneal epithelial cells. FF-SS-OCT has also been used to image *in-vivo* the human cornea [21,51], and digital refocusing was applied to extend the depth of focus. Currently, the main limitation of FF-SS-OCT is the low axial resolution associated with the relatively narrow spectral range of tunable laser technology. As an alternative design, the LS-SD-OCT proposed in this study combines a high spatial resolution, fast imaging speed, and relatively large FOV. Therefore it maybe more suitable for *in-vivo*, non-invasive, contactless, volumetric imaging of the cellular structure of human cornea and limbus.

In the B-scan image of the corneal epithelium (Fig. 3(B)), only the wing cells were resolved while the superficial cells and basal cells were not observed. The superficial cells were overwhelmed by the strong reflection signal of the interface of air and tear film, which can be reduced by asking the imaged subject to wear a contact lens. While the contact lens material will introduce additional dispersion in the OCT images, that can be easily compensated in post-processing. The missing of basal cells might be because the scattering coefficient is low [52]. Visualization of the basal cells may be achieved by improving the image SNR through averaging of multiple B-scans or 3D volumes and applying despeckling algorithms or other image enhancement algorithms. While the image SNR can also be increased by reducing the image acquisition rate or increasing the optical power of the imaging beam, these approaches are not advisable, as the current imaging power is already close to the MPE limit and slowing down the camera will introduce more image blur and eye motion artefacts.

In the magnified enface images of the corneal endothelium (Figs. 3(K) and 3(L)), dark spots were observed inside the endothelial cells. These dark dots most likely correspond to cellular nuclei. One might expect that since the refractive index of the endothelial nuclei is higher than the one of the cytoplasm, the nuclei will appear as "bright" rather than "dark" spots. However, the images shown in Figs. 3(J), 3(K) and 3(L) are generated by MIP from the 3D image stack and include the highly reflective interface between the posterior surface of the corneal endothelium and the fluid of the anteriour eye chamber. Since the strong specular reflection from that layer is stronger than the reflection from the cellular nuclei, the image contrast of the nuclei is reversed and they appear as "dark" spots over a more reflective background.

In both the B-scan and enface images of the limbus (Figs. 4 and 5), hyper-reflecting line structures were identified under the POVs. Anatomically, both blood vessels, extending along the POVs, as well as peripheral nerves, are located under the folds of the POVs, and both can reflect light strongly compared to the surrounding tissue. Further studies utilizing motion detection approaches such as Doppler OCT or optical micro-angiography (OMAG) to resolve moving particles from static scatterers are required to identify the nature of these reflective morphological features. Furthermore, limbal stem cells and early transient amplifying cells are characterized by significantly smaller size and tend to line up against the LC walls, compared to limbal epithelium

Biomedical Optics EXPRESS

cells which are larger in size and populate the bulk of the LC. Therefore, we speculate that the cells marked with the blue arrow in Fig. 5(D) are most likely limbal stem cells and/or early transient amplifying cells, though further studies are required to prove this hypothesis.

Although the novel LS-SD-OCT system has shown excellent research potential in clinical and biomedical imaging, there are still several limitations that need to be addressed in the future. First, the effective lateral FOV shown is ~700 × 700 μm, whereas the optical design allows ~1400 μm FOV in the y-direction. The reduced FOV is related to 2 factors: a) the optical power of the imaging beam has a Gaussian intensity distribution along the illumination line, which results in spatially dependent SNR within each B-scan, where the SNR is lower at the 2 ends of the frame relative to the central position along the line; b) the curved surface of the cornea results in lower image contrast at the 2 ends of the B-scan relative to the center, as less of the backscattered light is coupled into the NA of the imaging objective for locations where the curvature is stronger. The former problem can be resolved by shaping the Gaussian line into a uniformly illuminated line by using a Powell lens. This approach will ensure constant SNR across the lateral FOV and allow for use of the full FOV [53,54]. The latter problem can be compensated by correcting the defocus aberration, using a zero power contact lens over the cornea, or applying an curved scanning pattern of the corneal surface.

Next, in the current setup, both the digital resolution in the y-direction and the spectral resolution are not sufficiently high, according to the Nyquist sampling theorem. The low digital spatial resolution may cause aliasing, and the low spectral resolution results in a reduced OCT signal at a large depth. However, these two parameters cannot be increased simultaneously because of the contradiction of the sample to camera magnification in the horizontal and beam size entering the spectrometer in the vertical direction. This paradox can be resolved by replacing the doublets before the transmission grating with a pair of perpendicularly oriented cylindrical achromatic lenses [55]. Replacing the transmission grating, camera lens, and camera may also help resolve this problem.

Another problem we have not addressed yet is the spatial crosstalk within a B-scan. The confocal gate of the point-scanning OCT intrinsically rejects the multiply scattered light, while FF-TD-OCT and FF-SS-OCT reduce the crosstalk using the spatially incoherent light generated by light-emitting diode [19], random deformable mirror [27], or multimode fiber [51,56]. Spatially incoherent light generated with the multimode fiber and sparse sampling using a digital micromirror device might be two promising solutions to suppress the spatial crosstalk in LS SD-COT [57].

5. Conclusions

In conclusion, we have developed a novel LS-SD-OCT system that combines high spatial resolution and fast image acquisition, necessary for *in-vivo*, non-contact imaging of the cellular structure of the human cornea and limbus. We also show for the first time volumetric images of the cellular structure of the limbal crypts and the POVs acquired *in-vivo* and without contact from the healthy human limbus. When adopted for clinical use, the LS-SD-OCT can aid the diagnosing of potentially blinding corneal and limbal pathologies, monitoring the effectiveness of various treatments, and assist ophthalmic surgeons with pre-operative planning.

Funding. Canada First Research Excellence Fund; Canadian Institutes of Health Research (446387); Natural Sciences and Engineering Research Council of Canada (312037).

Acknowledgments. We thank the PCO America team for assistance with the Dimax S4 camera and Dr. A. Roorda for assistance with the head frame design.

Disclosures. The authors declare no conflicts of interest related to this article.

Data availability. Data underlying the results presented in this paper are not publicly available at this time but may be obtained from the authors upon reasonable request.

Biomedical Optics EXPRESS

References

1. M. S. Oliva, T. Schottman, and M. Gulati, "Turning the tide of corneal blindness," Indian J Ophthalmol **60**(5), 423–427 (2012).
2. R. L. Niederer and C. N. J. McGhee, "Clinical in vivo confocal microscopy of the human cornea in health and disease," Prog Retin Eye Res **29**(1), 30–58 (2010).
3. W. Drexler, "Ultrahigh-resolution optical coherence tomography," J Biomed Opt **9**(1), 47–74 (2004).
4. M. Ang, M. Baskaran, R. M. Werkmeister, J. Chua, D. Schmidl, V. A. dos Santos, G. Garhöfer, J. S. Mehta, and L. Schmetterer, "Anterior segment optical coherence tomography," Prog Retin Eye Res **66**, 132–156 (2018).
5. R. Yadav, K.-S. Lee, J. P. Rolland, J. M. Zavislan, J. V. Aquavella, and G. Yoon, "Micrometer axial resolution OCT for corneal imaging," Biomed. Opt. Express **2**(11), 3037–3046 (2011).
6. R. M. Werkmeister, A. Alex, S. Kaya, A. Unterhuber, B. Hofer, J. Riedl, M. Bronhagl, M. Vietauer, D. Schmidl, T. Schmoll, G. Garhöfer, W. Drexler, R. A. Leitgeb, M. Groeschl, and L. Schmetterer, "Measurement of Tear Film Thickness Using Ultrahigh-Resolution Optical Coherence Tomography," Investigative Opthalmology Vis Sci **54**(8), 5578 (2013).
7. P. Tankam, Z. He, Y.-J. Chu, J. Won, C. Canavesi, T. Lepine, H. B. Hindman, D. J. Topham, P. Gain, G. Thuret, and J. P. Rolland, "Assessing microstructures of the cornea with Gabor-domain optical coherence microscopy: pathway for corneal physiology and diseases," Opt. Lett. **40**(6), 1113 (2015).
8. K. Bizheva, L. Haines, E. Mason, B. MacLellan, B. Tan, D. Hileeto, and L. Sorbara, "In Vivo Imaging and Morphometry of the Human Pre-Descemet's Layer and Endothelium With Ultrahigh-Resolution Optical Coherence Tomography," Invest Ophth Vis Sci **57**(6), 2782 (2016).
9. K. Bizheva, B. Tan, B. MacLelan, O. Kralj, M. Hajialamdari, D. Hileeto, and L. Sorbara, "Sub-micrometer axial resolution OCT for in-vivo imaging of the cellular structure of healthy and keratoconic human corneas," Biomed. Opt. Express **8**(2), 800–812 (2017).
10. S. Chen, X. Liu, N. Wang, X. Wang, Q. Xiong, E. Bo, X. Yu, S. Chen, and L. Liu, "Visualizing Micro-anatomical Structures of the Posterior Cornea with Micro-optical Coherence Tomography," Sci Rep-uk **7**(1), 10752 (2017).
11. X. Yao, K. Devarajan, R. M. Werkmeister, V. A. dos Santos, M. Ang, A. Kuo, D. W. K. Wong, J. Chua, B. Tan, V. A. Barathi, and L. Schmetterer, "In vivo corneal endothelium imaging using ultrahigh resolution OCT," Biomed Opt Express **10**(11), 5675 (2019).
12. B. Tan, Z. Hosseinaee, L. Han, O. Kralj, L. Sorbara, and K. Bizheva, "250 kHz, 1.5 μm resolution SD-OCT for in-vivo cellular imaging of the human cornea," Biomed. Opt. Express **9**(12), 6569–6583 (2018).
13. A. Dubois, L. Vabre, A.-C. Boccara, and E. Beaurepaire, "High-resolution full-field optical coherence tomography with a Linnik microscope," Appl Optics **41**(4), 805 (2002).
14. A. Dubois, K. Grieve, G. Moneron, R. Lecaque, L. Vabre, and C. Boccara, "Ultrahigh-resolution full-field optical coherence tomography," Appl Optics **43**(14), 2874 (2004).
15. R. A. Leitgeb, "En face optical coherence tomography: a technology review [Invited]," Biomed Opt Express **10**(5), 2177–2201 (2019).
16. K. Grieve, M. Paques, A. Dubois, J. Sahel, C. Boccara, and J.-F. L. Gargasson, "Ocular tissue imaging using ultrahigh-resolution, full-field optical coherence tomography," Invest Ophth Vis Sci **45**(11), 4126 (2004).
17. M. Akiba, N. Maeda, K. Yumikake, T. Soma, K. Nishida, Y. Tano, and K. P. Chan, "Ultrahigh-resolution imaging of human donor cornea using full-field optical coherence tomography," J Biomed Opt **12**(4), 041202 (2007).
18. W. Ghouali, K. Grieve, S. Bellefqih, O. Sandali, F. Harms, L. Laroche, M. Paques, and V. Borderie, "Full-Field Optical Coherence Tomography of Human Donor and Pathological Corneas," Curr Eye Res **40**(5), 526–534 (2015).
19. V. Mazlin, P. Xiao, E. Dalimier, K. Grieve, K. Irsch, J.-A. A. Sahel, M. Fink, and A. C. Boccara, "In vivo high resolution human corneal imaging using full-field optical coherence tomography," Biomed. Opt. Express **9**(2), 557–568 (2018).
20. V. Mazlin, P. Xiao, J. Scholler, K. Irsch, K. Grieve, M. Fink, and C. A. Boccara, "Real-time non-contact cellular imaging and angiography of human cornea and limbus with common-path full-field/SD OCT," Nat Commun **11**(1), 1868 (2020).
21. E. Auksorius, D. Borycki, P. Stremplewski, K. Liżewski, S. Tomczewski, P. Niedźwiedziuk, B. L. Sikorski, and M. Wojtkowski, "In vivo imaging of the human cornea with high-speed and high-resolution Fourier-domain full-field optical coherence tomography," Biomed Opt Express **11**(5), 2849 (2020).
22. B. Považay, A. Unterhuber, B. Hermann, H. Sattmann, H. Arthaber, and W. Drexler, "Full-field time-encoded frequency-domain optical coherence tomography," Opt. Express **14**(17), 7661 (2006).
23. T. Bonin, G. Franke, M. Hagen-Eggert, P. Koch, and G. Hüttmann, "In vivo Fourier-domain full-field OCT of the human retina with 1.5 million A-lines/s," Opt. Lett **35**(20), 3432 (2010).
24. D. Hillmann, H. Spahr, C. Hain, H. Sudkamp, G. Franke, C. Pfäffle, C. Winter, and G. Hüttmann, "Aberration-free volumetric high-speed imaging of in vivo retina," Sci. Rep. **6**(1), 35209 (2016).
25. D. Hillmann, H. Spahr, H. Sudkamp, C. Hain, L. Hinkel, G. Franke, and G. Hüttmann, "Off-axis reference beam for full-field swept-source OCT and holoscopy," Opt. Express **25**(22), 27770–27784 (2017).
26. P. Stremplewski, E. Auksorius, P. Wnuk, Ł. Kozoń, P. Garstecki, and M. Wojtkowski, "In vivo volumetric imaging by crosstalk-free full-field OCT," Optica **6**(5), 608 (2019).
27. E. Auksorius, D. Borycki, and M. Wojtkowski, "Crosstalk-free volumetric in vivo imaging of a human retina with Fourier-domain full-field optical coherence tomography," Biomed Opt Express **10**(12), 6390 (2019).

Biomedical Optics EXPRESS

28. S. G. Adie, B. W. Graf, A. Ahmad, S. P. Carney, and S. A. Boppart, "Computational adaptive optics for broadband optical interferometric tomography of biological tissue," Proc National Acad Sci **109**(19), 7175–7180 (2012).
29. A. Kumar, W. Drexler, and R. A. Leitgeb, "Numerical focusing methods for full field OCT: a comparison based on a common signal model," Opt. Express **22**(13), 16061 (2014).
30. A. Kumar, T. Kamali, R. Platzer, A. Unterhuber, W. Drexler, and R. A. Leitgeb, "Anisotropic aberration correction using region of interest based digital adaptive optics in Fourier domain OCT," Biomed Opt Express **6**(4), 1124–1134 (2015).
31. D. Borycki, E. Auksorius, P. Węgrzyn, and M. Wojtkowski, "Computational aberration correction in spatiotemporal optical coherence (STOC) imaging," Opt. Lett **45**(6), 1293–1296 (2020).
32. A. Kumar, W. Drexler, and R. A. Leitgeb, "Subaperture correlation based digital adaptive optics for full field optical coherence tomography," Opt. Express **21**(9), 10850 (2013).
33. A. Zuluaga and R. Richards-Kortum, "Spatially resolved spectral interferometry for determination of subsurface structure," Opt. Lett. **24**(8), 519 (1999).
34. L. Ginner, A. Kumar, D. Fechtig, L. M. Wurster, M. Salas, M. Pircher, and R. A. Leitgeb, "Noniterative digital aberration correction for cellular resolution retinal optical coherence tomography in vivo," Optica **4**(8), 924–931 (2017).
35. V. P. Pandiyan, A. Maloney-Bertelli, J. A. Kuchenbecker, K. C. Boyle, T. Ling, Z. C. Chen, B. H. Park, A. Roorda, D. Palanker, and R. Sabesan, "The optoretinogram reveals the primary steps of phototransduction in the living human eye," Sci Adv **6**(37), eabc1124 (2020).
36. "ANSI Z80.36-2016 - Ophthalmics - Light Hazard Protection for Ophthalmic Instruments," https://webstore.ansi.org/standards/vc%20(asc%20z80)/ansiz80362016.
37. R. Watkins, "OpticStudio models of the human eye," https://support.zemax.com/hc/en-us/articles/1500005575082-OpticStudio-models-of-the-human-eye.
38. F. C. Delori, R. H. Webb, and D. H. Sliney, "Maximum permissible exposures for ocular safety (ANSI 2000), with emphasis on ophthalmic devices," J Opt Soc Am **24**(5), 1250 (2007).
39. M. J. Hogan, J. A. Alvarado, and J. E. Weddell, *Histology of the Human Eye: An Atlas and Textbook* (Saunders, 1971).
40. E. M. V. Buskirk, "The anatomy of the limbus," Eye **3**(2), 101–108 (1989).
41. H. S. Dua and A. Azuara-Blanco, "Limbal Stem Cells of the Corneal Epithelium," Surv Ophthalmol **44**(5), 415–425 (2000).
42. J. G. Lawrenson and G. L. Ruskell, "The structure of corpuscular nerve endings in the limbal conjunctiva of the human eye," J Anat **177**, 75–84 (1991).
43. P. A. R. Meyer, "The circulation of the human limbus," Eye **3**(2), 121–127 (1989).
44. E. B. Papas, "The limbal vasculature," Contact Lens Anterior Eye **26**(2), 71–76 (2003).
45. H. S. Dua, V. A. Shanmuganathan, A. O. Powell-Richards, P. J. Tighe, and A. Joseph, "Limbal epithelial crypts: a novel anatomical structure and a putative limbal stem cell niche," Brit J Ophthalmol **89**(5), 529–532 (2005).
46. M. F. Goldberg and A. J. Bron, "Limbal palisades of Vogt," T Am Ophthal Soc **80**, 155 (1982).
47. A. Wartak, M. S. Schenk, V. Bühler, S. A. Kassumeh, R. Birngruber, and G. J. Tearney, "Micro-optical coherence tomography for high-resolution morphologic imaging of cellular and nerval corneal micro-structures," Biomed Opt Express **11**(10), 5920 (2020).
48. W. Song, L. Chen, L. Han, A. R. Martinez, and K. Bizheva, "400kHz, 1 μm axial resolution SD-OCT for ophthalmic applications," Ophthalmic Technologies **Xxxii**, 3 (2022).
49. M. Münter, H. Schulz-Hildebrandt, M. Pieper, P. König, and G. Hüttmann, "4D microscopic optical coherence tomography imaging of ex vivo mucus transport," Opt. Coherence Imaging Techniques Imaging Scatt Media Iii **11078**, 11078115 (2019).
50. V. Mazlin, K. Irsch, M. Paques, J.-A. Sahel, M. Fink, and C. A. Boccara, "Curved-field optical coherence tomography: large-field imaging of human corneal cells and nerves," Optica **7**(8), 872 (2020).
51. E. Auksorius, D. Borycki, and M. Wojtkowski, "Multimode fiber enables control of spatial coherence in Fourier-domain full-field optical coherence tomography for in vivo corneal imaging," Opt. Lett. **46**(6), 1413 (2021).
52. Y.-T. Chen, C.-Y. Tsai, Y.-K. Chiu, T.-W. Hsu, L. W. Chen, W.-L. Chen, and S.-L. Huang, "En face and cross-sectional corneal tomograms using sub-micron spatial resolution optical coherence tomography," Sci Rep-uk **8**(1), 14349 (2018).
53. I. Powell, "Design of a laser beam line expander," Appl Optics **26**(17), 3705 (1987).
54. Z. Al-Qazwini, Z. Ko, K. Mehta, and N. Chen, "Ultrahigh-speed line-scan SD-OCT for four-dimensional in vivo imaging of small animal models," Biomed. Opt. Express **9**(3), 1216–1228 (2018).
55. V. P. Pandiyan, X. Jiang, A. Maloney-Bertelli, J. A. Kuchenbecker, U. Sharma, and R. Sabesan, "High-speed adaptive optics line-scan OCT for cellular-resolution optoretinography," Biomed Opt Express **11**(9), 5274 (2020).
56. A.-H. Dhalla, J. V. Migacz, and J. A. Izatt, "Crosstalk rejection in parallel optical coherence tomography using spatially incoherent illumination with partially coherent sources," Opt. Lett. **35**(13), 2305 (2010).
57. J. Lu, B. Gu, X. Wang, and Y. Zhang, "High speed adaptive optics ophthalmoscopy with an anamorphic point spread function," Optics express **26**(11), 14356–14374 (2018).